Journal of Materials Chemistry A

ROYAL SOCIETY OF CHEMISTRY

PAPER

View Article Online
View Journal | View Issue

Cite this: J. Mater. Chem. A, 2021, 9, 19840

Mesoporous titanium niobium nitrides supported Pt nanoparticles for highly selective and sensitive formaldehyde sensing†

Chaozhu Huang,‡[bc] Samira Adimi,‡[a] Dongliang Liu,[b] Haichuan Guo,[b] Tiju Thomas,[d] J. Paul Attfield,[e] Shengping Ruan,*[a] Fengdong Qu*[ab] and Minghui Yang*[bc]

A proton exchange membrane fuel cell (PEMFC) gas sensor is a promising and novel gas sensing device. However, the poor sensitivity and strong cross sensitivity of commercial carbon-supported-platinum (Pt/C) remain obstacles to its utilization. Here, we demonstrate that the issue can be addressed using mesoporous titanium niobium nitrides ($Ti_{0.75}Nb_{0.25}N$) synthesized using a solid–solid phase separation process. Pt nanoparticles supported on ternary transition metal nitrides enable the strong metal support interaction (SMSI), which changes the surface electronic structure and catalytic activity of the electrode material. Compared with the Pt/C-sensor, the selectivity of the Pt/$Ti_{0.75}Nb_{0.25}N$-based sensor to formaldehyde (HCHO) is significantly higher, while the response to other gases is effectively inhibited. In mixed gas tests, HCHO sensing of the Pt/$Ti_{0.75}Nb_{0.25}N$-sensor is still not affected (within 3.5% of the standard deviation limit). Furthermore, the Pt/$Ti_{0.75}Nb_{0.25}N$-sensor exhibits a much higher sensitivity (0.208 μA per ppm) toward HCHO when compared to the Pt/C-sensor (0.058 μA per ppm). The Pt/$Ti_{0.75}Nb_{0.25}N$-sensor also exhibits extraordinary long-term stability due to its electrochemical stability and SMSI of the electrode material. This work hence points to the design and development of a new sensing electrode system, which offers a combination of high selectivity and sensitivity when used in fuel-cell gas sensors.

Received 24th March 2021
Accepted 30th April 2021

DOI: 10.1039/d1ta02433g

rsc.li/materials-a

Introduction

Toxic and harmful gases/vapors pose significant potential risks to human and ecological health.[1–3] This is also a concern in indoor environments which have relatively slow air circulation and air replacement.[4,5] Formaldehyde, which is classified as a Group I human carcinogen by IARC (International Agency for Research on Cancer), is a common and dangerous indoor air pollutant.[6] Inhaled formaldehyde is rapidly absorbed in the respiratory tract and gastrointestinal tract.[7] It reacts with nucleophilic compounds in the body due to its high solubility in aqueous solvents and electrophilic properties.[8] This stimulates the eyes, nasal mucosa, alveoli and immune system, and leads to a series of adverse effects such as rhinitis, pulmonary edema and even leukemia.[9–11] The threshold value of formaldehyde is recommended to be 100 ppb according to ACGIH (American Conference of Governmental Industrial Hygienists).[12] However, the lowest level of human sensory stimulation is 400–500 ppb.[13] Currently liquid chromatography and spectrophotometry are often used to detect trace amounts of formaldehyde in air.[14] However, these instruments are accompanied by a series of shortcomings, such as being time-consuming, associated with high costs and complicated processes.[15,16] In this context, it is indispensable to develop an *in situ* formaldehyde detection equipment with high sensitivity, good selectivity and wide detection range.[17]

Proton exchange membrane fuel cell (PEMFC) type gas sensors have been considered as one of the most promising gas detection equipment due to their low power consumption (in fact it has no need for external voltage and works at room temperature), low cost associated along with features such as portability, good linear signal and fast response.[18,19] In order to ensure practical benefits of the PEMFC in the field of gas sensing, the following problems of Pt/C electrode materials must be solved: (i) poor selectivity to target gas, (ii) low

[a]State Key Laboratory on Integrated Optoelectronics, College of Electronic Science and Engineering, Jilin University, Changchun, 130012, China. E-mail: ruansp@jlu.edu.cn
[b]Ningbo Institute of Materials Technology & Engineering, Chinese Academy of Sciences, Ningbo, 315201, China
[c]Center of Materials Science and Optoelectronics Engineering, University of Chinese Academy of Sciences, Beijing 100049, China
[d]Department of Metallurgical and Materials Engineering, Indian Institute of Technology Madras, Adyar, Chennai 600036, India
[e]Centre for Science at Extreme Conditions, School of Chemistry, University of Edinburgh, King's Buildings, May field Road, Edinburgh, EH93JZ, UK

† Electronic supplementary information (ESI) available. See DOI: 10.1039/d1ta02433g

‡ These authors contributed equally to this work.

sensitivity and (iii) sensitivity drift during long-term operation.[20] Recently, various efforts have been attempted to surmount these challenges. The modification of carbon support materials affects the surface electronic structure of Pt nanoparticles, such as acid treated carbon fibers, graphene-carbon black hybrid and S-doped carbon layer.[21–23] Although this strategy can effectively improve the performance of fuel cells, it still has the limitations of stability and selectivity due to the weak metal-support interaction. In addition, the synergistic effect of binary metal catalysts is also investigated. For example, Pt–Sn/C,[24] Pt–Ni/C[25] Pt–Cu/C[26] and Pt_xPd_y/C[27] can be used to improve the gas sensing performance of sensors. However, the compositional segregation of Pt alloy nanoparticles and the poor electrochemical stability of carbon will aggravate the sensitivity drift of the sensor during long-term operation.[28] To this end, Lu, Yang and Wei *et al.* developed finely dispersed iron hydroxide clusters anchored on Pt which enhance the selectivity of fuel cells.[29] This almost meets the requirements of ideal electrode materials due to the strong metal support interaction, good electrochemical stability and no compositional segregation, except for the complex process, high cost and low yield in the synthesis of the atomic scale support.

Transition metal nitrides (TMNs) have been extensively studied as high-performance catalysts in various applications, including electrocatalysts,[30,31] capacitors,[32] Zn–air cells,[33] and fuel cells[34] due to their high conductivity, high catalytic activity and thermal and electrochemical stability.[35,36] Particularly, some mesoporous transition metal nitrides such as TiN[37] and WN[20] are known to possess outstanding co-catalytic properties and can effectively replace the carbon black support to improve the gas sensing performance of fuel cell gas sensors. The porous nature not only ensures the uniform dispersion of Pt nanoparticles, but also provides sufficient number of channels and active sites for gas diffusion and adsorption.[38,39] To further improve the 3S (selectivity, sensitivity and stability) sensing index of electrode sensing materials, a feasible scheme is to regulate the composition of TMNs.

Ternary TMNs with appropriate composition offer superior performance as a catalyst support material which surpasses the advantages offered by binary nitrides.[40] For instance, mesoporous $Ti_{0.5}Cr_{0.5}N$ can act as a highly active catalyst support for the electro-oxidation of formic acid and methanol.[41] This is ascribed to the strong metal-support interactions at the interface. The combination of noble metal and support transforms the adsorption energy and catalytic activity of the detection gas on the catalyst surface, thus improving the selective catalysis of specific molecules.[42] The appropriate surface electronic structure constructed by strong bonding links promotes the concentration-dependent response of the sensor.

Herein, we investigate the mesoporous titanium niobium nitrides as the support material of the sensing electrode to improve the selectivity and sensitivity of fuel cell gas sensors. By replacing carbon black with best performing ternary nitrides with nominal composition – $Ti_{0.75}Nb_{0.25}N$ – as the support of Pt, enables a significant improvement in formaldehyde gas sensing performance. $Pt/Ti_{0.75}Nb_{0.25}N$ exhibits desirable formaldehyde selectivity with negligible cross sensitivity to other interfering gases/vapors. The sensitivity (0.208 μA per ppm) is 3.6 times higher than that of commercial Pt/C (0.058 μA per ppm). In addition, the limit of detection (LoD) is 100 ppb, and the sensor's long term tolerance is found to be excellent (99% of the initial value after two months of continuous operation).

Experimental section

Materials

Zinc oxide (ZnO, 99%), isopropanol (anhydrous, 99.5%), methanol (CH_3OH, 99%), ethanol (C_2H_5OH, 99%) and ethylene glycol (anhydrous, 99%) are purchased from Sinopharm Chemical Reagent Co., Ltd (Shanghai, China). Titanium oxide (TiO_2, 99%), niobium oxide (Nb_2O_5, 99.9%), formaldehyde (HCHO, 37 wt%), carbon disulfide (CS_2, 99.9%) and chloroplatinic acid hexahydrate ($H_2PtCl_6 \cdot 6H_2O$, 99.9%) are purchased from Aladdin (Shanghai, China). The commercial Platinum Black on Carbon Black (Pt/C, 20 wt% Pt) is purchased from Johnson Matthey (Shanghai, China). Hydrogen (H_2, 99.9%) and carbon monoxide (CO, 99%) are purchased from Wanli Gas Chemical Co., Ltd (Ningbo, China).

Materials synthesis and device fabrication

Preparation of mesoporous $Ti_xNb_{1-x}N$. Five mesoporous nitrides with different Ti, Nb stoichiometric ratios are synthesized by a solid–solid separation method. The solid solutions of metal oxide precursors (MOPs) are prepared by preheating specific metal oxides of ZnO, TiO_2, and Nb_2O_5 at 600 °C and 1250 °C for 6 h and 8 h. $Ti_xNb_{1-x}N$ is prepared using ammonolysis of 0.4–0.8 g MOPs in a quartz boat. The boat is put into a ceramic pipe with a sealing ring. The end-caps are connected with the welding valve to link the pipeline to both the input and output of gas. Anhydrous high-purity ammonia gas is introduced into the tubular furnace with air removed by a vacuum pump. The MOP is heated to 850 °C for 12 h to form corresponding nitrides and the sample is cooled to room temperature in 3–5 h under an ammonia flow. Prior to the removal of the ceramic tube from the tubular furnace, argon is introduced to discharge ammonia to prevent back suction. The ceramic tube with a slight opening is placed in the laboratory for 24 h to slowly expose the ammonolysis products to air.

Preparation of $Pt/Ti_xNb_{1-x}N$. First, 50 mg $Ti_xNb_{1-x}N$ is suspended in 50 ml ethylene glycol and dispersed by ultrasonic stirring. 33.2 mg H_2PtCl_6 is added to the above suspension, and it is then sonicated in an ice water bath. The suspension is subjected to a hydrothermal reaction at 140 °C for 3 h. Subsequently, the suspension is vacuum filtered using Nylon-66 filter membranes, and the precipitate is washed with deionized water and alcohol. And then, the powders obtained are dried at 60 °C overnight to obtain the product. The actual Pt loading of $Ti_{0.75}Nb_{0.25}N$ and Pt/C(JM) are 17.7 wt% and 17.2 wt% (ICP), respectively.

Sensor fabrication. 5 mg $Ti_xNb_{1-x}N$ and 40 μL of 5 wt% Nafion (DUPONT, USA.) are added into 800 μl isopropanol and deionized water, and the catalyst ink is obtained using ultrasonication. The ink is loaded onto the surface of carbon paper

(Shanghai Hesen Co., Ltd) by air spraying at 90 °C. Then, two sheets of carbon paper are combined with a Nafion N115 membrane (DUPONT, USA.). Two pieces of the PTFE membrane are used as a protective layer and are hot pressed at 90 °C and 1 MPa for 120 s. After that, the PTFE membrane is torn off and the membrane electrode assembly (MEA) is obtained. The MEA is cut to match the size of the brass electrode (1.0 cm in diameter). It is then combined with the brass electrode by hot melt adhesive to form a small fuel cell. Then, the cathode of the sensor is sealed with a water container containing absorbent cotton soaked in deionized water. During the operation of the sensor, the counter electrode is sealed in the isolation chamber filled with wet air, and the working electrode is exposed to the external target gas.

Characterization

X-ray powder diffraction (XRD) is carried out using a powder X-ray diffractometer (Rigaku MiniFlex 600, Japan) with Cu K_α radiation at $\lambda = 1.5418$ Å, scanning speed: 0.1° min^{-1}, and 2θ range of 10–85°. The surface morphology of the material is studied using a scanning electron microscope (SEM) (Verios G4 UC, USA). High-resolution transmission electron microscopy (HRTEM) and high-angle annular dark field scanning transmission electron microscopy (HAADF-STEM) are performed using a Talos F200× (America). X-ray photoelectron spectroscopy (AXIS SUPRA, UK) is used to analyze the atomic chemical valence states of the contaminated sample surface. The actual content of platinum in $Ti_{0.75}Nb_{0.25}N$ and commercial platinum–carbon is determined using an inductively coupled plasma emission spectrometer (SPECTROARCOS II, Germany). Brunauer–Emmett–Teller (BET) analysis of $Ti_{0.75}Nb_{0.25}N$ is performed by using an automatic specific surface area and micropore analyzer (ASAP2020HD88, America).

Gas sensing measurements

Fig. S1† shows the real picture and schematic diagram of the test system. A multichannel potentiostat (CHI1030C, Shanghai Chenhua Instrument Co., Ltd) is used to test the gas sensing performance in the chronoamperometry mode at zero potential applied. All sensors are kept at 95% humidity for 24 h before connecting them to the working circuit. The anode and cathode of the gas sensor are respectively connected to the working electrode, counter electrode and reference electrode, and no other electrical equipment is connected. Before gas sensing, the sensor operates in air for 5–10 min to obtain a stable reference current (I_0). The difference between the gas sensing current (I_G) and I_0 is defined as the response current (ΔI). The sensitivity of the sensor is the linear fitting slope between ΔI and gas concentration. When the sensor is put into or taken out of the gas, the current change value is 90% of the ΔI value, which is defined as the response recovery time. The protons and electrons produced by the gas electrode reaction are conducted through a Nafion membrane and external circuit, respectively. The response value and response recovery time of the sensor correspond to the type and concentration of the gas. Therefore, the multi-channel voltage regulator is used to collect the current signal as a function of time to analyze the performance of the sensor. All gases/vapors to be measured in this work are from commercial high purity gases or solutions. The concentration of the target gas is prepared by using the gas distribution formula (see the ESI† for details), and the air is used as the background gas. Except for the experiments to explore the influence of humidity, all the tests are conducted at 25 °C and 50% RH.

Results and discussion

The PEMFC gas sensor is a symmetrical layered structure composed of two metal electrodes, two gas diffusion layers, two gas sensing layers and a solid electrolyte membrane (Fig. 1).The gas diffusion layer not only ensures the efficient gas diffusion, but also supports and protects the catalyst of the sensing layer and maintains the shape of the MEA.[43] The sensing layer composed of the electrode catalyst ($Pt/Ti_{0.75}Nb_{0.25}N$ in this work) is in close contact with the solid electrolyte through an ionomer (Nafion solution in this work). The target gas is catalytically oxidized at the three-phase interface of the sensing layer, and the generated protons are conducted to the counter electrode by the Nafion membrane. For obtaining mesoporous $Ti_xNb_{1-x}N$ deposited with Pt nanoparticles, Zn containing molten precursors are first heated under a flow of ammonia gas to reduce the metal oxides to mesoporous nitrides. The formation of mesoporous nitride materials is due to the evaporation loss of Zn, and three oxygen anions are replaced by two nitrogen anions. During the ammonolysis process, the oxide precursor loses oxygen and forms water, resulting in the condensation of nanoscale voids and further sintering to obtain the mesoporous structure. Following this, Pt nanoparticles are deposited by reducing chloroplatinic acid ($H_2PtCl_6 \cdot 6H_2O$) with ethylene glycol. After the reaction, we obtain free-flowing black crystalline powders of $Pt/Ti_xNb_{1-x}N$ (Fig. S2 and Table S1, ESI†).

The Rietveld-refined powder XRD pattern of $Ti_{0.75}Nb_{0.25}N$ and $Pt/Ti_{0.75}Nb_{0.25}N$ confirms the successful synthesis of ternary crystalline nitrides and Pt NPs. The diffraction peaks of the samples are indexed by the face centered cubic structure (space group: $Fm\bar{3}m$), and the cell parameters respectively are $a = 4.249(4)$ Å ($Ti_{0.75}Nb_{0.25}N$), $a = 3.925(3)$ Å (Pt), residuals wR = 10.97%, and $R = 8.27\%$ (Fig. 2a). To confirm the detailed surface chemical states of the catalyst, we carried out X-ray photoelectron spectroscopy analysis (Fig. S3, ESI†). The spectra are modified with the C 1s reference at a binding energy

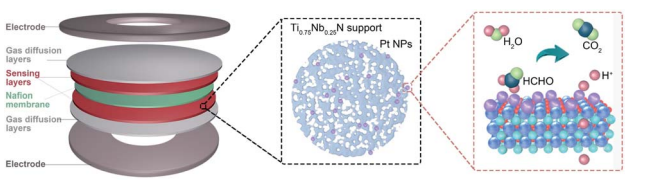

Fig. 1 Structure and performance characteristics of the proton exchange membrane fuel cell (PEMFC) gas sensor. Left: schematic illustration of the PEMFC sensor. Middle: microstructure of the sensing layer of the working electrode. Right: gas sensing at the working electrode (take formaldehyde detection as an example).

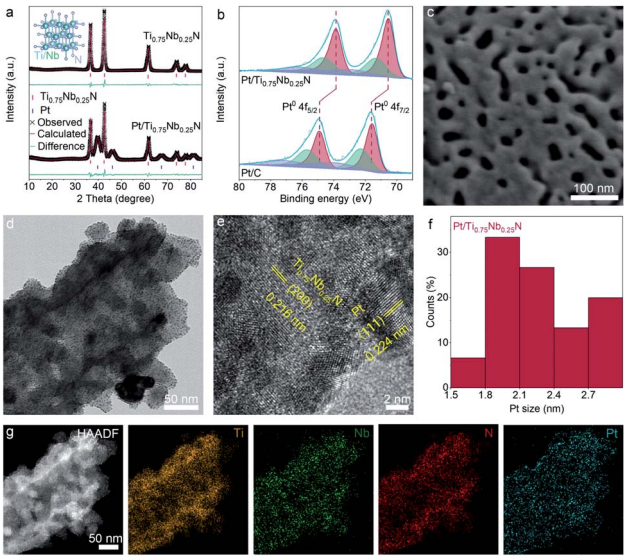

Fig. 2 (a) The Rietveld fitted powder X-ray diffraction pattern of $Ti_{0.75}Nb_{0.25}N$ and $Pt/Ti_{0.75}Nb_{0.25}N$. (b) X-ray photoelectron spectroscopy spectra of $Pt/Ti_{0.75}Nb_{0.25}N$ and Pt/C (Johnson Matthey) in the Pt 4f region. (c) SEM images of $Ti_{0.75}Nb_{0.25}N$. (d) TEM images of $Pt/Ti_{0.75}Nb_{0.25}N$ and (e) HRTEM image of $Pt/Ti_{0.75}Nb_{0.25}N$. (f) Pt size distribution of $Pt/Ti_{0.75}Nb_{0.25}N$. (g) HAADF-STEM image and corresponding EDX mapping images of Ti, Nb, N and Pt.

of 284.8 eV. Fig. 2b shows the high-resolution Pt 4f spectra of $Pt/Ti_{0.75}Nb_{0.25}N$ and Pt/C. The relative area of Pt (0), *i.e.* the integral strength in the $Pt/Ti_{0.75}Nb_{0.25}N$ catalyst is larger than that of the Pt/C catalyst, which is conducive to improve the catalytic activity of the sensing electrode.[44] Compared with the Pt/C catalyst, the Pt 4f (0) bonding energy of $Pt/Ti_{0.75}Nb_{0.25}N$ has a negative shift of about 0.98 eV. This confirms the strong interaction between Pt and $Ti_{0.75}Nb_{0.25}N$.[45] The negative shift of the binding energy indicates that the nitrides support supply electrons to Pt nanoparticles. This leads to the change of the surface electronic structure of Pt, which enhances the gas sensing response and provides a suitable electronic structure.[46]

The porosity of the support material is further confirmed by scanning electron microscopy (SEM), as shown in Fig. 2c and S4.† It is obvious that mesoporous nitrides with a pore size of about 10–30 nm have been formed. This is a well-known range of the effective mesoporous size and can significantly promote the gas diffusion characteristics. The results of transmission electron microscopy (TEM) and high-resolution TEM (HRTEM) image indicate that the crystalline Pt nanoparticles are uniformly deposited on the surface of the support material (Fig. 2d and e). And samples with a lattice fringe of 2.16 Å for the (200) plane of $Ti_{0.75}Nb_{0.25}N$ and 2.24 Å for the (111) plane of Pt are detected. As illustrated in Fig. 2f, we calculated the Pt NP size distribution of $Pt/Ti_{0.75}Nb_{0.25}N$ and its average diameter is concentrated in the range of 1.5–3 nm. The high-angle annular dark-field scanning TEM (HAADF-STEM) image of the catalyzer and the corresponding EDX mapping image of Ti, Nb, N and Pt elements (Fig. 2g) reveal a similar and uniform distribution, further indicating that ternary nitrides are successfully synthesised and Pt NPs are uniformly loaded.

A large number of interconnected pores indicate that the surface of $Pt/Ti_{0.75}Nb_{0.25}N$ has good gas accessibility due to its porous nature.[47] This result can be verified by Brunauer–Emmett–Teller (BET) analysis (Fig. S5, ESI†). The specific surface area and pore distribution of electrode materials are analyzed by nitrogen adsorption and desorption isotherms at 77 K. The results indicate that $Ti_{0.75}Nb_{0.25}N$ shows type IV isotherms with H3 hysteresis loops and the Barrett–Joyner–Halenda (BJH) surface area is 37.4 $m^2\ g^{-1}$. The pore size distribution is mainly in the range of 10–30 nm, and the average pore size is 23.1 nm. This indicates the existence of mesopores formed by Zn^{2+} reduction and sublimation. The support materials with large specific surface area significantly increase the gas sensing reaction sites and gas channels of the catalyst. In addition, the abundant mesoporous structure is also conducive to the transmission of water vapor, which is necessary for the normal operation of the fuel cell sensor, thus reducing the dependence of the sensor on external humidity.[48,49] Combining the results of SEM, TEM and BET analysis, the mesoporous $Ti_{0.75}Nb_{0.25}N$ with high volume specific surface area and high gas accessibility is an ideal support for Pt NPs.

In order to clearly verify the influence of nitride composition on gas sensing characteristics, we prepared five electrode catalyst supports with different Ti and Nb element ratios for formaldehyde gas sensing. The dynamic sensing transients of $Pt/Ti_xNb_{1-x}N$ sensors toward 50 ppm formaldehyde are shown in Fig. 3a and S6.† The response of ternary nitrides to 50 ppm HCHO is significantly higher than that of the corresponding binary nitride. This indicates that the ternary nitrides with a more complex electronic structure exhibits better co-catalytic

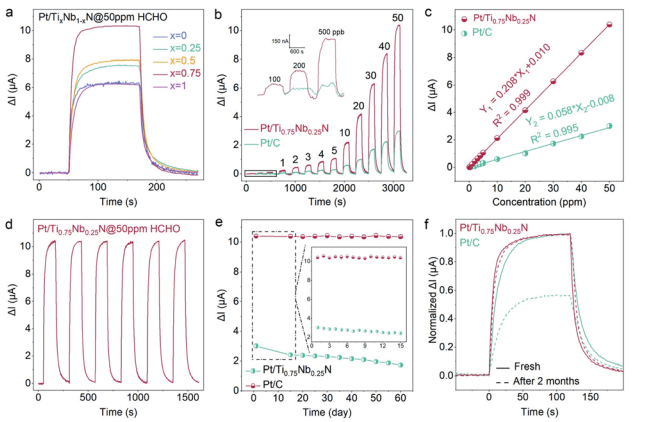

Fig. 3 (a) The response transients of the $Pt/Ti_xNb_{1-x}N$ sensor to 50 ppm formaldehyde. (b) Real-time responses and (c) formaldehyde concentration dependent response value of $Pt/Ti_xNb_{1-x}N$ and Pt/C sensors to 0.1–50 ppm formaldehyde. (d) The 6-cycle dynamic sensor response verifies the repeatability of the $Pt/Ti_{0.75}Nb_{0.25}N$ sensor to 50 ppm formaldehyde. (e) Comparison of response attenuation of $Pt/Ti_{0.75}Nb_{0.25}N$ and Pt/C-based sensors in detecting 50 ppm formaldehyde within two months. (f) Normalized real-time responses of $Pt/Ti_{0.75}Nb_{0.25}N$ and Pt/C-based sensors to 50 ppm formaldehyde at different aging states.

activity for formaldehyde sensing. Interestingly, $Ti_{0.75}Nb_{0.25}N$ exhibits the highest response to 50 ppm HCHO. The suitable composition of the ternary nitride can greatly enhance the catalytic oxidation of formaldehyde on the anode of the sensor. The greatly enhanced sensing performance may be due to the strong interaction between $Ti_{0.75}Nb_{0.25}N$ and Pt, which is conducive to the transfer of more electrons from the support to the Pt, leading to the catalytic oxidation of the gas.[44]

To clearly compare the sensing characteristics of the Pt/$Ti_{0.75}Nb_{0.25}N$-based sensor and Pt/C-based sensor toward formaldehyde, responses to various concentration (from 100 ppb to 50 ppm) are measured (Fig. 3b). Delightfully, the Pt/$Ti_{0.75}Nb_{0.25}N$ sensor performs well in the ranges of ppm and ppb. Furthermore, the response of the Pt/$Ti_{0.75}Nb_{0.25}N$ sensor is 2.97–4.36 times higher than that of the Pt/C sensor at the same concentration of formaldehyde. The response current of the Pt/$Ti_{0.75}Nb_{0.25}N$ sensor and Pt/C sensor in various concentrations of formaldehyde is fitted linearly, and the function of ΔI for the concentration is obtained, as shown in Fig. 3c. Both the sensors exhibit a superlative linear response to formaldehyde in the range of 100 ppb to 50 ppm; however the sensitivity of the Pt/$Ti_{0.75}Nb_{0.25}N$ sensor (0.208 μA per ppm) is much higher than that of the Pt/C sensor (0.058 μA per ppm).

The LoD of Pt/$Ti_{0.75}Nb_{0.25}N$ and Pt/C is obtained by exposing the sensors to formaldehyde vapor with increasing concentration and measuring the current of the circuit. According to the inset of Fig. 3b, the LoD of Pt/$Ti_{0.75}Nb_{0.25}N$ is 100 ppb, while Pt/C lacks recognizable response signals in formaldehyde of 200 ppb. In order to further verify the potential of the sensor for ppb-level formaldehyde, we explore its theoretical LoD by using the root mean square deviation (RMSD) method.[50] ESI Fig. S7† shows the baseline current of Pt/$Ti_{0.75}Nb_{0.25}N$ and Pt/C sensors operating in air for 20 minutes, and the noise (σ) of the current signal is calculated to be 0.26 nA and 0.59 nA, respectively. The theoretical LoD is defined as $3\sigma/S$ (S is the sensitivity of the sensor) by the signal-to-noise ratio (SNR), and the calculated results of Pt/$Ti_{0.75}Nb_{0.25}N$ and Pt/C sensors are 3.7 ppb and 30.5 ppb, respectively. The enhancement of the LoD is attributed to the following: (i) low current fluctuation is beneficial to obtain a recognizable response signal, and (ii) the strong interaction between the support and metal promotes the oxidation of gas adsorbed on the catalyst surface.

The signal attenuation of sensors during long-term operation is a long-standing problem, which greatly reduces the sensor accuracy and service life and increases the risk of unreliable sensing results.[51] The stability of the Pt/$Ti_{0.75}Nb_{0.25}N$ sensor for formaldehyde detection is demonstrated using a repeatability test and long-term tolerance test. As shown in Fig. 3d, the response variation of the sensor in 6 cycles of 50 ppm formaldehyde detection is less than 0.7%. The average real-time response of the repeatability detection maintains good consistency in all cycles with only slight deviations (Fig. S8a†). This verifies the reliable repeatability of the sensor for formaldehyde detection.

When these sensors are subjected to long-term stability tests for 60 days, the variation curves of ΔI for 50 ppm formaldehyde are presented in Fig. 3e. The Pt/$Ti_{0.75}Nb_{0.25}N$ sensor exhibits excellent long-term stability (maintaining 99% of the initial response) with only slight fluctuation of ΔI during the two-month tolerance test. This may be attributed to its strong interaction, which can significantly inhibit the aggregation and desorption of Pt, resulting in outstanding stability and durability. By comparison, the Pt/C sensor suffers serious fluctuation and attenuation in the first 15 days of the test, and the response proceeds to further continuously drop in the next 45 days. Therefore, the sensor only maintains 57% of the initial performance after 2 months. As shown in Fig. 3f, the normalized real-time sensing transient of Pt/$Ti_{0.75}Nb_{0.25}N$ after 2 months basically coincides with the initial response (the response and recovery time lag slightly), while Pt/C is significantly attenuated and scrapped.

The real-time and rapid detection of target gas also depend on the response and recovery characteristics of the sensor. The ΔI–t curves of the Pt/$Ti_{0.75}Nb_{0.25}N$ and Pt/C sensor to 50 ppm formaldehyde are shown in Fig. 4a. The response and recovery time of Pt/$Ti_{0.75}Nb_{0.25}N$ are 14 s and 19 s, respectively, which are only 37% and 33% that of commercial Pt/C (38 s and 57 s). This exhibits obvious advantages for formaldehyde detection, especially for electrochemical sensors working at room temperature. The sensing characteristics of formaldehyde gas sensors reported in recent years are summarized in Table S2† and this work exhibits advantages of stability, sensitivity and rapid detection.

To verify that the Pt/$Ti_{0.75}Nb_{0.25}N$ sensor is superior to the Pt/C sensor in selectivity, we conducted the experiment on 50 ppm formaldehyde (HCHO), methanol (CH_3OH), ethanol (C_2H_5OH), hydrogen (H_2), carbon monoxide (CO) and carbon disulfide (CS_2) under the same conditions (Fig. 4b). The response current of Pt/$Ti_{0.75}Nb_{0.25}N$ to 50 ppm formaldehyde is 10.43 μA, which is

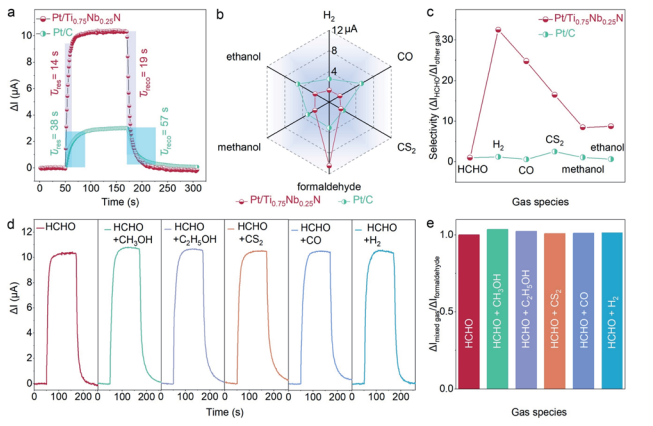

Fig. 4 (a) Real time response transient of Pt/$Ti_{0.75}Nb_{0.25}N$ and Pt/C sensors to 50 ppm formaldehyde (HCHO). (b) Selectivity and (c) selectivity improvements for Pt/$Ti_{0.75}Nb_{0.25}N$ and Pt/C sensors toward various analyte gases. (d) Sensor response of Pt/$Ti_{0.75}Nb_{0.25}N$ to a transient of 50 ppm formaldehyde followed by five transients of mixed gases of 50 ppm formaldehyde and 50 ppm methanol (CH_3OH), 50 ppm ethanol (C_2H_5OH), 50 ppm carbon disulfide (CS_2), 50 ppm carbon monoxide (CO) and 50 ppm hydrogen (H_2), respectively. (e) The response of the sensor fluctuates only slightly during exposure to different gas mixtures.

significantly higher than the other interfering gases/vapors (0.32–1.23 μA). However, the response of the Pt/C sensor to some interfering gases (CO and C_2H_5OH) is higher than that of formaldehyde. Hence the strong cross sensitivity hinders its practicability. We intuitively confirm that Pt/$Ti_{0.75}Nb_{0.25}N$ exhibit better selectivity for formaldehyde by calculating the improved selectivity ($\Delta I_{HCHO}/\Delta I_{other\ gas}$) of the sensor (Fig. 4c). The above clearly indicate that $Ti_{0.75}Nb_{0.25}N$ as a catalyst support can effectively enhance the formaldehyde sensing and inhibit the response of other gases. The increase in selectivity of the Pt/$Ti_{0.75}Nb_{0.25}N$ sensor may be due to the change of adsorption and electrochemical activity of the catalyst for different gases.[52] By controlling the composition of support materials, a more complex surface electronic structure can be constructed and the synergistic effect between the catalyst and support materials can be increased.[53] This changes the gas adsorption at the three-phase reaction interface and the catalytic activity of gas sensing materials for different gases.

For practical applications, poor selectivity in complex detection scenarios is prone to false alarms.[54] Fig. 4d shows the transient response of Pt/$Ti_{0.75}Nb_{0.25}N$ to 50 ppm formaldehyde and a mixture of 50 ppm formaldehyde and 50 ppm interfering gas. The response of the sensor to mixed gas is within 3.5% of the standard deviation limit for 50 ppm formaldehyde (Fig. 4e). It is obvious that the sensor has the feasibility of the highly selective detection of formaldehyde under realistic conditions.

The SMSI is the key factor for the excellent selectivity, sensitivity, LoD and stability of the Pt/$Ti_{0.75}Nb_{0.25}N$ sensor. In order to further verify the SMSI between Pt and the support, density functional theory (DFT) is used to explore the formation energy (Fig. S10†). The formation energy between $Ti_{0.75}Nb_{0.25}N$ and Pt (−2.41 eV) is obviously smaller than that between C and Pt (2.16 eV). Low formation energy contributes to electron transfer, which improves the stability and SMSI of the gas sensing catalyst.[55]

In addition, relative humidity (RH) is another important factor that can be explored to affect the gas sensing performance of the sensor.[56–58] As shown in Fig. S11,† the response of the sensor to 50 ppm formaldehyde at different RH (11%, 33%, 55%, 75% and 95%) is detected. According to the comparison of response transients and ΔI under different humidity conditions, RH has little effect on the performance of the sensor. The signal drift of the sensor is less than 6% of the initial value when the ΔI of 11% RH is selected as the reference. This may be due to the fact that the sensor is equipped with a cathode sealed chamber, and its high humidity gas can effectively soak the MEA. Therefore, the performance of the sensor is less affected by the external humidity.

Conclusions

In summary, we successfully synthesized mesoporous $Ti_{0.75}Nb_{0.25}N$ as a new catalyst support for fuel cell gas sensors. The sensing electrode catalyst provides a strong combination of selectivity and sensitivity enhancement due to the strong metal support interaction between Pt and the support. The response of the sensor to formaldehyde is outclassed by other interfering gases, and it still maintains a unique sensing ability to formaldehyde in mixed gases. Its sensitivity is 3.6 times higher than that of commercially available Pt/C, and it has a good linear correlation between ΔI and concentration for 100 ppb to 50 ppm. Furthermore, the inherent electrochemical stability of the support material provides the sensor with negligible signal fluctuations and sensitivity drifts during long-term operation.

Conflicts of interest

There are no conflicts to declare.

Acknowledgements

This work is supported by the Natural Science Foundation of China (Grant No. 61971405), National Key Research and Development Plan of China (Grant No. 2016YFB0101205) and the Science and Technology Foundation of Ningbo, China (Grant No. 2019C50010). M. Y. would like to thank the National "Thousand Youth Talents" program of China and the Ningbo 3315 program for support. J. P. A. thanks the EPSRC for support. T. T. thanks the DST of India for financial support for work on energy harnessing (*via* DSEHC), Indo-Hungarian project, Core research grant and materials for energy storage and conversion (*via* MES).

Notes and references

1 J.-Y. Kang, J.-S. Jang, W.-T. Koo, J. Seo, Y. Choi, M.-H. Kim, D.-H. Kim, H.-J. Cho, W. Jung and I.-D. Kim, *J. Mater. Chem. A*, 2018, **6**, 10543–10551.
2 D. Xu, P. Xu, X. Wang, Y. Chen, H. Yu, D. Zheng and X. Li, *ACS Appl. Mater. Interfaces*, 2020, **12**, 8091–8097.
3 T. Yang, Y. Huo, Y. Liu, Z. Rui and H. Ji, *Appl. Catal., B*, 2017, **200**, 543–551.
4 R. Malik, V. K. Tomer, T. Dankwort, Y. K. Mishra and L. Kienle, *J. Mater. Chem. A*, 2018, **6**, 10718–10730.
5 S. Rong, P. Zhang, F. Liu and Y. Yang, *ACS Catal.*, 2018, **8**, 3435–3446.
6 J. Ji, X. Lu, C. Chen, M. He and H. Huang, *Appl. Catal., B*, 2020, **260**, 118210.
7 G. D. Nielsen, S. T. Larsen and P. Wolkoff, *Arch. Toxicol.*, 2017, **91**, 35–61.
8 T. Salthammer, *Angew. Chem., Int. Ed. Engl.*, 2013, **52**, 3320–3327.
9 D. Yan, P. Xu, Q. Xiang, H. Mou, J. Xu, W. Wen, X. Li and Y. Zhang, *J. Mater. Chem. A*, 2016, **4**, 3487–3493.
10 K. Wu, X. Y. Kong, K. Xiao, Y. Wei, C. Zhu, R. Zhou, M. Si, J. Wang, Y. Zhang and L. Wen, *Adv. Funct. Mater.*, 2019, **29**, 1807953.
11 Q. Liang, X. Qu, N. Bai, H. Chen, X. Zou and G. D. Li, *J. Hazard. Mater.*, 2020, **400**, 123301.
12 C. Lou, C. Yang, W. Zheng, X. Liu and J. Zhang, *Sens. Actuators, B*, 2021, **329**, 129218.
13 T. Salthammer, S. Mentese and R. Marutzky, *Chem. Rev.*, 2010, **110**, 2536–2572.

14 Z. Jin, P. Li, G. Liu, B. Zheng, H. Yuan and D. Xiao, *J. Mater. Chem. A*, 2013, **1**, 14736.
15 J. L. Wang, Y. J. Guo, G. D. Long, Y. L. Tang, Q. B. Tang, X. T. Zu, J. Y. Ma, B. Du, H. Torun and Y. Q. Fu, *J. Hazard. Mater.*, 2020, **388**, 121743.
16 X. Sun, H. Zhang, L. Huang, S. Hao, J. Zhai and S. Dong, *Biosens. Bioelectron.*, 2021, **177**, 112975.
17 H. Yu, J. Li, W. Luo, Z. Li, Y. Tian, Z. Yang, X. Gao and H. Liu, *Appl. Surf. Sci.*, 2020, **513**, 145825.
18 E. Jayanthi, N. Murugesan, S. Anthonysamy and C. Ramesh, *Sens. Actuators, B*, 2018, **273**, 488–497.
19 A. Modjtahedi, A. Amirfazli and S. Farhad, *Sens. Actuators, B*, 2016, **234**, 70–79.
20 D. Meng, S. Zhang, T. Thomas, C. Huang, J. Zhao, R. Zhao, Y. Shi, F. Qu and M. Yang, *Sens. Actuators, B*, 2020, **307**, 127686.
21 Y. Guan, F. Liu, B. Wang, X. Yang, X. Liang, H. Suo, P. Sun, Y. Sun, J. Ma, J. Zheng, Y. Wang and G. Lu, *Sens. Actuators, B*, 2017, **239**, 696–703.
22 K. Ham, S. Chung and J. Lee, *J. Power Sources*, 2020, **450**, 227650.
23 I. H. Lee, J. Cho, K. H. Chae, M. K. Cho, J. Jung, J. Cho, H. J. Lee, H. C. Ham and J. Y. Kim, *Appl. Catal., B*, 2018, **237**, 318–326.
24 X. Yang, W. Li, Y. Zhang, T. Liu, X. Hao, R. Zhou, X. Liang, F. Liu, F. Liu, Y. Gao, X. Yan and G. Lu, *Sens. Actuators, B*, 2019, **299**, 126972.
25 W. Li, X. Yang, Y. Zhang, X. Hao, T. Liu, X. Liang, F. Liu, X. Yan, F. Liu, Y. Gao, J. Ma and G. Lu, *Sens. Actuators, B*, 2020, **311**, 127900.
26 W. Li, Y. Zhang, X. Hao, Y. Zhang, X. Yang, X. Liang, F. Liu, X. Yan, S. Zhang and G. Lu, *Sens. Actuators, B*, 2020, **311**, 127905.
27 E. Jayanthi, N. Murugesan and C. Ramesh, *Microchem. J.*, 2020, **156**, 104851.
28 C. Cui, L. Gan, M. Heggen, S. Rudi and P. Strasser, *Nat. Mater.*, 2013, **12**, 765–771.
29 L. Cao, W. Liu, Q. Luo, R. Yin, B. Wang, J. Weissenrieder, M. Soldemo, H. Yan, Y. Lin, Z. Sun, C. Ma, W. Zhang, S. Chen, H. Wang, Q. Guan, T. Yao, S. Wei, J. Yang and J. Lu, *Nature*, 2019, **565**, 631–635.
30 H. Shen, L. Pan, T. Thomas, J. Wang, X. Guo, Y. Zhu, K. Luo, S. Du, H. Guo, G. J. Hutchings, J. P. Attfield and M. Yang, *Cell Rep. Phys. Sci.*, 2020, **1**, 100255.
31 Y. Yuan, S. Adimi, X. Guo, T. Thomas, Y. Zhu, H. Guo, G. S. Priyanga, P. Yoo, J. Wang, J. Chen, P. Liao, J. P. Attfield and M. Yang, *Angew. Chem., Int. Ed. Engl.*, 2020, **59**, 18036–18041.
32 S. Li, T. Wang, Y. Huang, Z. Wei, G. Li, D. H. L. Ng, J. Lian, J. Qiu, Y. Zhao, X. Zhang, J. Ma and H. Li, *ACS Appl. Mater. Interfaces*, 2019, **11**, 24114–24121.
33 X. X. Yu, T. P. Zhou, J. K. Ge and C. Z. Wu, *ACS Mater. Lett.*, 2020, **2**, 1423–1434.
34 J. Zheng, W. Zhang, J. Zhang, M. Lv, S. Li, H. Song, Z. Cui, L. Du and S. Liao, *J. Mater. Chem. A*, 2020, **8**, 20803–20818.
35 Y. Liu, D. Tian, A. N. Biswas, Z. Xie, S. Hwang, J. H. Lee, H. Meng and J. G. Chen, *Angew. Chem., Int. Ed. Engl.*, 2020, **59**, 11345–11348.
36 Y. Yuan, J. Wang, S. Adimi, H. Shen, T. Thomas, R. Ma, J. P. Attfield and M. Yang, *Nat. Mater.*, 2020, **19**, 282–286.
37 D. Meng, S. Zhang, T. Thomas, R. Zhao, Y. Shi, F. Qu and M. Yang, *Sens. Actuators, B*, 2020, **308**, 127713.
38 G. Wang, J. Qin, X. Zhou, Y. Deng, H. Wang, Y. Zhao and J. Wei, *Adv. Funct. Mater.*, 2018, **28**, 1806144.
39 R. Kim, J. S. Jang, D. H. Kim, J. Y. Kang, H. J. Cho, Y. J. Jeong and I. D. Kim, *Adv. Funct. Mater.*, 2019, **29**, 1903128.
40 M. Yang, A. R. Van Wassen, R. Guarecuco, H. D. Abruna and F. J. DiSalvo, *Chem. Commun.*, 2013, **49**, 10853–10855.
41 Z. M. Cui, M. H. Yang and F. J. DiSalvo, *ACS Nano*, 2014, **8**, 6106–6113.
42 S. Yao, L. Lin, W. Liao, N. Rui, N. Li, Z. Liu, J. Cen, F. Zhang, X. Li, L. Song, L. Betancourt De Leon, D. Su, S. D. Senanayake, P. Liu, D. Ma, J. G. Chen and J. A. Rodriguez, *ACS Catal.*, 2019, **9**, 9087–9097.
43 J. T. S. Allan, H. L. Geoffrey and E. B. Easton, *Sens. Actuators, B*, 2018, **254**, 120–132.
44 Y. Xiao, Z. Fu, G. Zhan, Z. Pan, C. Xiao, S. Wu, C. Chen, G. Hu and Z. Wei, *J. Power Sources*, 2015, **273**, 33–40.
45 M. Roca-Ayats, G. García, J. L. Galante, M. A. Peña and M. V. Martínez-Huerta, *J. Phys. Chem. C*, 2013, **117**, 20769–20777.
46 G. Liu, Z. Pan, B. Zhang, J. Xiao, G. Xia, Q. Zhao, S. Shi, G. Hu, C. Xiao, Z. Wei and Y. Xu, *Int. J. Hydrogen Energy*, 2017, **42**, 12467–12476.
47 S. Y. Jeong, Y. K. Moon, J. K. Kim, S. W. Park, Y. K. Jo, Y. C. Kang and J. H. Lee, *Adv. Funct. Mater.*, 2020, **31**, 2007895.
48 Z. Duan, Q. Zhao, S. Wang, Q. Huang, Z. Yuan, Y. Zhang, Y. Jiang and H. Tai, *Sens. Actuators, B*, 2020, **317**, 128204.
49 Z. Duan, Q. Zhao, S. Wang, Z. Yuan, Y. Zhang, X. Li, Y. Wu, Y. Jiang and H. Tai, *Sens. Actuators, B*, 2020, **305**, 127534.
50 F. Qu, Y. Yuan, R. Guarecuco and M. Yang, *Small*, 2016, **12**, 3128–3133.
51 D. Zhao, H. Huang, S. Chen, Z. Li, S. Li, M. Wang, H. Zhu and X. Chen, *Nano Lett.*, 2019, **19**, 3448–3456.
52 B. Song, D. Choi, Y. Xin, C. R. Bowers and H. Hagelin-Weaver, *Angew. Chem., Int. Ed. Engl.*, 2021, **60**, 4038–4042.
53 Q. Zhou, K. Yu, Z. Pan, Z. Huang, Y. Xu, G. Hu, S. Wu, C. Chen, L. Lin and Y. Lin, *Int. J. Hydrogen Energy*, 2018, **43**, 22519–22528.
54 F. Qu, S. Zhang, C. Huang, X. Guo, Y. Zhu, T. Thomas, H. Guo, J. P. Attfield and M. Yang, *Angew. Chem., Int. Ed. Engl.*, 2021, **60**, 6561–6566.
55 X. Wang, A. Beck, J. A. van Bokhoven and D. Palagin, *J. Mater. Chem. A*, 2021, **9**, 4044–4054.
56 H. Tai, Z. Duan, Z. He, X. Li, J. Xu, B. Liu and Y. Jiang, *Sens. Actuators, B*, 2019, **298**, 126874.
57 Y. Zhang, J. Zhang, Y. Jiang, Z. Duan, B. Liu, Q. Zhao, S. Wang, Z. Yuan and H. Tai, *Sens. Actuators, B*, 2020, **319**, 128293.
58 Q. Zhao, Z. Duan, Z. Yuan, X. Li, W. Si, B. Liu, Y. Zhang, Y. Jiang and H. Tai, *Chin. Chem. Lett.*, 2020, **31**, 2045–2049.

